

Numerical studies of domains and bubbles of Langmuir monolayers

Kok-Kiong Loh and Joseph Rudnick

Department of Physics, UCLA, Los Angeles, California 90095-1547

(Received 9 February 2000)

A numerical algorithm based on the finite element method has been developed to accurately determine the shape of the boundary of a domain containing “boojum” textures, which are order-parameter distributions that resemble the structure of the orbital angular momentum in a superfluid ^3He droplet [N.D. Mermin, in *Quantum Fluids and Solids*, edited by S.B. Trickey, E. Adams, and J. Duffy (Plenum, New York, 1997)]. Within the context of the simple model we adopt, the effects of both bulk elastic anisotropy and line-tension anisotropy on the domain boundary can be examined. It is found that line-tension anisotropy must be present in order to account for domains with protruding features. Both elastic anisotropy and anisotropic line tension can result in domains with indentations. The numerical algorithm has been extended to investigate the problem of a bubble in an extended region ordered phase.

PACS number(s): 68.55.-a, 68.18.+p, 68.55.Ln, 68.60.-p

I. INTRODUCTION

A Langmuir monolayer is a single molecular layer of insoluble surfactant molecules spread on the air/water interface. The surfactants are typically amphiphilic molecules with a hydrophilic headgroup and a hydrophobic tail. Each of the individual molecules has internal degrees of freedom, namely, the tilt and the tilt azimuth. Such a system exhibits a complex phase diagram [1]. The “tilted” phases have uniform tilt and possess mesoscopic ordering in the tilt azimuth. The structure of the tilt azimuth is typically observed as a variation in the light intensity under a Brewster angle microscope. The tilt azimuth organization is referred to as the texture. Various classes of the texture have been observed, such as stripes in the bulk [2], star configurations [3,4], and “boojums” [5] in the domains of the tilted phase, when it coexists with an isotropic phase. The term boojum refers to a class of textures that has a tilt azimuth distribution which resembles the structure of the orbital angular momentum in a superfluid ^3He droplet [6]. The boojum texture, in which the tilt azimuth is distributed continuously without singularity, will be the subject of this report. Domains observed to contain a boojum texture are not circular in shape [5,7]. In addition, micrometer-sized bubbles, which are regions of isotropic phase surrounded by a tilted phase, have been found to have noncircular shapes [7]. The local tilt azimuth in the tilted phase around the bubble exhibits a nontrivial structure, which has been termed an “inverse boojum.” The relationship between experimentally observed textures and the underlying structure of the ordered phase has attracted attention in the literature recently. In particular, the boojum texture was first discussed by Mermin in the context of orbital angular momentum distribution in a superfluid ^3He droplet [6]. Similar textures have been found and discussed in liquid crystal films [8,9]. An extensive discussion of the various classes of textures in the Langmuir monolayers can be found in Ref. [4].

The problem of the equilibrium shape of, and the texture contained in, domains in a Langmuir monolayer has been investigated by Rudnick and Bruinsma [10], who varied both the texture and the boundary analytically in a perturbative

manner. It was discovered that a noncircular boundary represents the equilibrium shape of a domain only when there is bulk or higher-order line-tension anisotropy [5,10]. The equilibrium domain boundary was derived as a function of line-tension anisotropy. Galatola and Fournier [11] obtained numerically, in a fixed background texture, the equilibrium boundary when both elastic and line-tension anisotropies are present. Rivière and Meunier [5] have attempted to explain the observed noncircular domains in terms of elastic anisotropy. Evidence of bubbles with a noncircular boundary and an inverse boojum has been reported, and a qualitative theoretical discussion of the equilibrium shape and texture associated with the bubbles can be found in Ref. [7]. In the spirit of Ref. [10], the authors have analyzed in Ref. [12] the equilibrium texture and boundary shape combinations perturbatively to first order in both the bulk elastic and line-tension anisotropies. The approach describes the infinitesimal response of the texture and the boundary to anisotropic parameters. However, when the correction is large enough to be observed, the validity of first-order perturbative calculations becomes questionable. The extension of the perturbative approach to include higher-order corrections is algebraically formidable. If one is to go beyond first-order effects, the use of numerical techniques in this problem is inevitable.

The major challenges in this problem are, first, the evaluation of a two-dimensional (2D) texture with a boundary condition on the boundary, which is itself variable. Secondly, not only must the texture be evaluated with high accuracy, but a precise determination of the derivatives of the texture on the boundary is also crucial to the computation of the boundary shape. The authors have developed a numerical algorithm based on the finite element method (FEM) with adaptive mesh refinement [13] for the evaluation of a 2D texture and its derivatives. The boundary corrections can then be computed using the Runge-Kutta method [14]. Implementation of the numerical method reveals various classes of domain shapes ranging from those with indentations to those with protruding features and, additionally, cigar-shaped domains. The effects of bulk elastic anisotropy have also been examined. These studies lead us to the conclusion that, at least for those domain shapes observed to

date, it is more likely that the line-tension anisotropy is responsible for noncircular domains. A brief account of the study described above has appeared in an earlier publication [15]. The numerical results reported there and in this paper confirm that the qualitative conclusions to be drawn from the perturbative treatment are preserved up to large anisotropic parameter.

In this paper, we describe in detail the implementation of the numerical methods that led us to the results reported in Ref. [15]. The extension of the algorithm to allow for computation in the case of a bubble has also been examined. It is verified numerically that bubbles acquire a nontrivial boundary shape when only the first term in the Fourier expansion of the line tension is present. This result contrasts with what is known to be true in the case of the domain, which remains circular in the presence of this low-order line-tension anisotropy [10]. With the use of our numerical algorithm, we are able to examine the effects of the bulk elastic anisotropy on the shape of the bubble and on the texture that surrounds it. We find that bulk elastic anisotropy significantly affects the texture in the condensed phase around the bubble while leaving the boundary nearly unmodified.

The organization of this paper is as follows. Section II contains the details of the computational scheme for the evaluation of the equilibrium textural and boundary configuration for domains. The discussion covers the derivation of the simplest variational formulation of the finite element method in our specific application, the Runge-Kutta method, and the combined algorithm. In Sec. III, results for the domain are examined. Section IV describes the extension of the numerical algorithm to the problem of bubbles. An examination of the results of the perturbative treatment follows. Results on the effect of the bulk elastic anisotropy on the textures around the bubbles are discussed. Finally, Sec. V contains concluding remarks and discusses possible future extensions of the numerical methods discussed in this report.

II. NUMERICAL ALGORITHM

The model that we adopt for the Langmuir monolayer is a simple elastic model of an ordered medium associated with XY -like order parameter—a two-dimensional unit vector $\hat{c}(x,y)$, which can be parametrized as $\hat{x}\cos\Theta(x,y) + \hat{y}\sin\Theta(x,y)$ [12]. The quantities \hat{x} and \hat{y} are unit vectors in a Cartesian coordinate system, and $\Theta(x,y)$ is the angle between \hat{c} and the x axis. The energy of the system contains contributions from the boundary Γ in addition to the bulk Ω . The most general form of the elastic energy [4,8] for such a system with in-plane reflection symmetry (an achiral system) can be written as

$$H[\Theta] = \int_{\Omega} \mathcal{H}_b dA + \oint_{\Gamma} \sigma(\vartheta - \Theta) ds, \quad (2.1)$$

where

$$\mathcal{H}_b = \frac{K_s}{2} |\nabla \cdot \hat{c}|^2 + \frac{K_b}{2} |\nabla \times \hat{c}|^2, \quad (2.2)$$

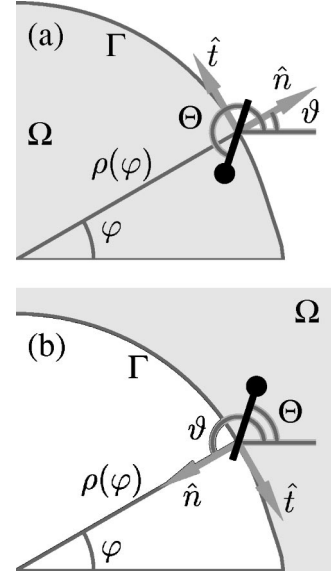


FIG. 1. The geometry of the calculations for (a) domains and (b) bubbles in plane-polar coordinates where the boundary Γ is parametrized by $\rho(\varphi)$. The gray area is the bulk designated by Ω . \hat{n} and \hat{t} are the outward normal and the tangent, respectively. Θ is the angle between the \hat{c} director and the x axis and ϑ is the angle between the outward normal of the boundary and the x axis.

$$\sigma(\phi) = \sigma_0 + \sum_{n=1} a_n \cos n\phi, \quad (2.3)$$

K_s and K_b are respectively the splay and bend elastic moduli, and ϑ is the angle between the outward normal \hat{n} of Γ and the x axis. The setup of the computations is shown in Fig. 1. In terms of the average Frank modulus κ and the coefficient of elastic anisotropy b , where $2\kappa \equiv K_b + K_s$ and $2\kappa b \equiv K_s - K_b$, the extrema of the elastic energy Eq. (2.1) occur when $\Theta(x,y)$ and the bounding curve Γ satisfy their respective equilibrium conditions. The extremum equations for $\Theta(x,y)$ are

$$-\nabla^2\Theta + b[(\Theta_{xx} - \Theta_{yy})\cos 2\Theta + 2\Theta_{xy}\sin 2\Theta + (-\Theta_x^2 + \Theta_y^2)\sin 2\Theta + 2\Theta_x\Theta_y\cos 2\Theta] = 0 \quad (2.4)$$

in Ω and

$$\kappa\Theta_n[1 - b\cos 2(\vartheta - \Theta)] + \kappa b\Theta_t \sin 2(\vartheta - \Theta) - \sigma'(\vartheta - \Theta) = 0 \quad (2.5)$$

along Γ , where $\Theta_n = \hat{n} \cdot \nabla\Theta$, $\Theta_t = \hat{t} \cdot \nabla\Theta$, \hat{t} being the tangential vector. The extremum equation for the bounding curve Γ , in terms of Θ_n , Θ_t , and $d\vartheta/ds$, is

$$\mathcal{H}_b - \sigma'(\vartheta - \Theta)\Theta_n - \sigma''(\vartheta - \Theta)\Theta_t + [\sigma(\vartheta - \Theta) + \sigma''(\vartheta - \Theta)]\frac{d\vartheta}{ds} + \lambda = 0, \quad (2.6)$$

where ds is the length element of Γ traversing in the positive direction of Ω , and λ is a Lagrange multiplier that enforces the condition of constant enclosed area.

The equations for both Θ and Γ are complex and highly nonlinear. Closed form analytic solution of the extremum equations appears impossible. Attempts have been made to solve the simultaneous equation perturbatively to first order in the elastic and line-tension anisotropies [12]. When the corrections to the boundaries are large enough to be observable, it is not expected that the results will be accurate and high-order corrections have to be taken into account. However, these perturbative calculations provide us with insight with regard to the infinitesimal response of the boundary to the anisotropies under investigation. In the work to be described below, we analyze the equations numerically in order to further explore the implications of the simple model Eq. (2.1) for a larger range of the anisotropic parameters. We retain coefficients up to a_2 in the expansion of the line tension in our analysis, i.e., $\sigma(\phi) = \sigma_0 + a_1(\cos \phi + \gamma \cos 2\phi)$, where the quantity $\gamma \equiv a_2/a_1$ is defined for convenience. We remark that the analysis will be based on the exact boojum texture with circular domain when $\gamma = b = 0$. The boundary will be computed in terms of the corrections to the circular boundary. The discussions will be restricted to those domains with boundaries Γ for which the distance from each point on the curves to the origin $e^{k(\varphi)}$ is a single-valued function of the polar angle φ .

The numerical algorithm consists of two parts: in the first part, one evaluates the texture Θ using an assumed boundary Γ , and, in the second part, one computes Γ using a fixed Θ . Simultaneous equilibrium conditions for Γ and Θ are achieved when a set of predefined self-consistent criteria are met. It is evident from the form of Eq. (2.6) that accurate determinations of Θ and its derivatives are the key factors in the solution of the problem. There are a number of numerical techniques for solving the partial differential equation Eq. (2.4), such as finite difference methods, spectral methods, finite element methods, etc. Both finite difference methods and spectral methods are convenient when applied to systems with boundaries of regular geometries, such as circles or straight lines, while the finite element methods are formulated for problems with highly irregular geometries. For the case of our problem, the boundary condition Eq. (2.5) applies to Γ , which is an arbitrary curve. This militates in favor of the FEM. A key feature of the FEM is flexibility in the choice of the set of points at which the functional values are to be evaluated, including those on the boundary of the region of interest. This feature is exactly what is needed in our problem, because of the nontrivial geometry of the boundary. One of the simplest constructions of the FEM in two dimensions is described as follows [13]. We first approximate Γ by a polygonal curve, then subdivide Ω into a set of nonoverlapping triangles. No vertex of one triangle lies on the edge of another in the set. The edges of the set of triangle form a mesh that covers Ω . The process of creating this set of triangles is called mesh generation. The resulting set of triangles is referred to as the triangulation of Ω . Functions are defined by their values on the vertices of the triangles in the triangulation. The value of a function within a triangle is obtained by interpolation using the values on the vertices. Integration over Ω is the sum of integrations over the tri-

angles, which can generally be trivially evaluated. We have now projected our problem, originally on an infinite dimensional space, onto an N dimensional space, where N is the number of vertices in the triangulation of Ω . We may write $\Theta \equiv (\Theta_i), i = 1, \dots, N$ and

$$\Theta(x, y) = \sum_{i=1}^N \Theta_i \varphi_i(x, y), \tag{2.7}$$

where $\varphi_i(x, y)$ is a set of basis functions of the N dimensional space. These φ_i 's should not be confused with the polar angle, which is denoted by the symbol φ without a subscript. The discrete version of the elastic energy functional Eq. (2.1) is a function of N variables Θ_i and it can be rewritten in terms of κ and b as

$$H(\Theta) = \frac{\kappa}{2} \int_{\Omega} \{ |\nabla \Theta|^2 + b [(-\Theta_x^2 + \Theta_y^2) \cos 2\Theta - 2\Theta_x \Theta_y \sin 2\Theta] \} dA + \oint_{\Gamma} \sigma(\vartheta - \Theta) ds, \tag{2.8}$$

where $\Theta_x = \sum \Theta_i \varphi_{ix}$, $\Theta_y = \sum \Theta_i \varphi_{iy}$, $\varphi_{ix} \equiv \partial \varphi_i / \partial x$, and $\varphi_{iy} \equiv \partial \varphi_i / \partial y$. The equilibrium condition becomes

$$\frac{\partial H(\Theta)}{\partial \Theta_i} = 0, \quad i = 1, \dots, N, \tag{2.9}$$

which is a discretized version of Eqs. (2.4) and (2.5). The set of equations above is not linear. However, if we write them in the form of $\mathbf{A}(\Theta) \cdot \Theta = \mathbf{b}(\Theta)$, where $\mathbf{A}(\Theta)$ is an $N \times N$ matrix, and $\mathbf{b}(\Theta)$ and Θ are $1 \times N$ column matrices as shown below:

$$A_{ij}(\Theta) = \kappa \int_{\Omega} [\varphi_{ix} \varphi_{jx} (1 - b \cos 2\Theta) + \varphi_{iy} \varphi_{jy} (1 + b \cos 2\Theta) + b(\varphi_{ix} \varphi_{jy} + \varphi_{iy} \varphi_{jx}) \sin 2\Theta] dA, \tag{2.10}$$

$$b_i(\Theta) = \kappa b \int_{\Omega} [(-\Theta_x^2 + \Theta_y^2) \sin 2\Theta + 2\Theta_x \Theta_y \cos 2\Theta] \varphi_i dA + \oint_{\Gamma} \sigma'(\vartheta - \Theta) \varphi_i ds, \tag{2.11}$$

we are able to solve for Θ iteratively using a standard numerical algorithm for the solution of systems of linear equations. We have adopted the method of LU decomposition [14], a numerical algorithm for inverting a matrix, to solve for Θ

The mesh generation algorithm plays an important role in the efficiency of the FEM. An adaptive mesh generation algorithm is used in our program to determine Θ . We start with a mesh that is nearly regular throughout Ω with a predefined grid size. After obtaining a first estimate of Θ , a refined mesh is generated. The refined mesh has variable grid sizes over Ω depending on the variation of Θ . Figure 2 depicts the process of mesh generation with adaptive refinement. We are able to determine not only Θ , but also the derivatives Θ_i and Θ_n , which are necessary for evaluating

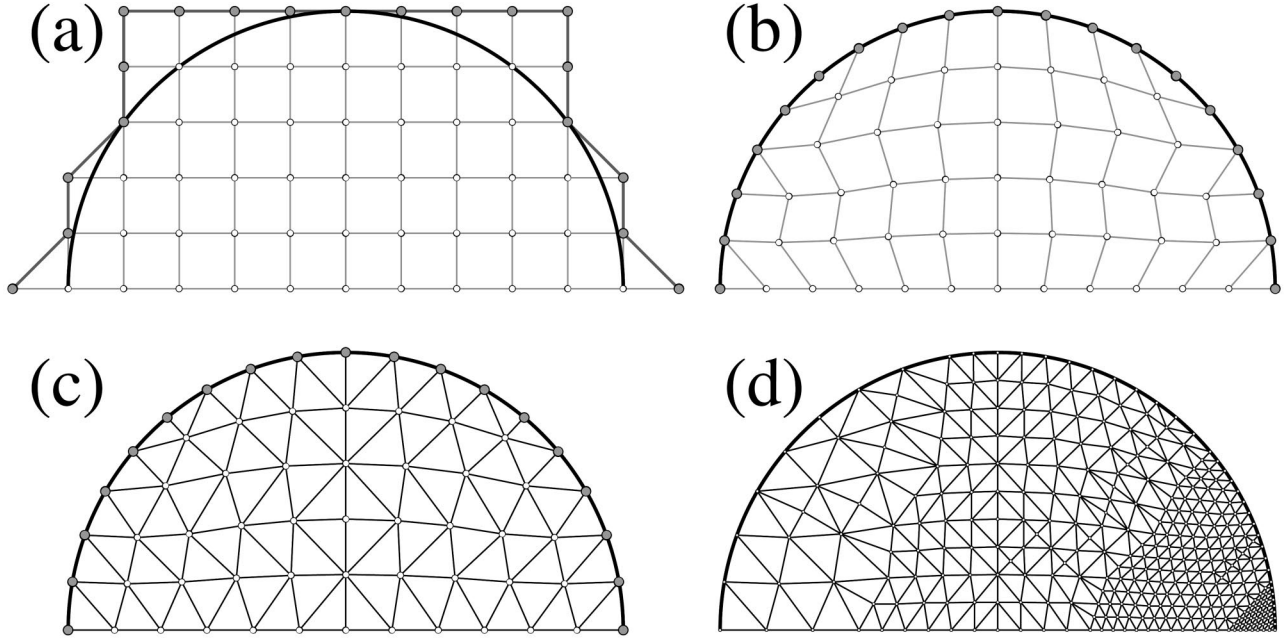


FIG. 2. The progressive steps toward mesh generation of the problem for the domain; (a) initial choice of grid points in a square lattice, (b) deforming to grid points into the region of interest Ω and the bounding curve Γ while keeping the square lattice topology and connectivity, (c) triangulation using the square lattice connectivity, and (d) resulting mesh after adaptive mesh refinement.

the bounding curve, accurately and efficiently with the adaptive mesh generation algorithm.

The next part of the algorithm is the determination of the bounding curve Γ . We assume the order parameter field Θ is fixed in Eq. (2.6) so as to simplify the problem. We then pick an origin in Ω and parametrize the bounding curve Γ as $k(\varphi)$, where $e^{k(\varphi)} \equiv |\mathbf{r}|$ is the distance between the origin and (x, y) on Γ , and φ is the polar angle. In this parametrization, Eq. (2.6) is a second-order nonlinear differential equation in $k(\varphi)$. If we rewrite Eq. (2.6) as

$$k'' + q(\varphi; k, k')k' = r(\varphi; k, k') \quad (2.12)$$

where $k' \equiv dk/d\varphi$ and

$$q(\varphi; k, k') = - \frac{\sigma' \Theta_\varphi - \sigma'' \Theta_k}{\sigma + \sigma''} (1 + k'^2), \quad (2.13)$$

$$r(\varphi; k, k') = \left(1 - \frac{\sigma' \Theta_k + \sigma'' \Theta_\varphi}{\sigma + \sigma''} \right) (1 + k'^2) + \frac{e^k \mathcal{H}_b + \lambda}{\sigma + \sigma''} (1 + k'^2)^{3/2}. \quad (2.14)$$

Again, it is possible to integrate the equation for $k(\varphi)$ iteratively using a standard method for the solution of ordinary differential equation. The Runge-Kutta method [14] is chosen for our application.

The problem of solving Eqs. (2.4), (2.5), and (2.6) for $\Theta(x, y)$ and Γ is reformulated in terms of the solution of Eqs. (2.9) and (2.12) iteratively for Θ and Γ . We begin by assuming an initial boundary $\Gamma^{(0)}$ and texture $\Theta^{(0)}$, from which the texture $\Theta^{(1)}$ can be computed using the FEM. Then the iterated texture $\Theta^{(1)} = \Theta^{(0)} + (\Theta^{(1)} - \Theta^{(0)})/\nu_T^{(0)}$ is

in turn used to evaluate a new accepted boundary $\Gamma^{(1)} = \Gamma^{(0)} + (\Gamma^{(1)} - \Gamma^{(0)})/\nu_B^{(0)}$, where $\Gamma^{(1)}$ is obtained using the Runge-Kutta ordinary differential equation integrator on Eq. (2.6). The process is repeated until both $\Delta \Theta^{(n)} \equiv |\Theta^{(n)} - \Theta^{(n-1)}|$ and $\Delta \Gamma^{(n)} \equiv |\Gamma^{(n)} - \Gamma^{(n-1)}|$ are less than a preset tolerance of the order $O(10^{-5})$. The factors $\nu_T^{(n)}$ and $\nu_B^{(n)}$ with initial magnitude on the order of $O(10)$ are introduced to avoid numerical instability in these iterative processes. These factors, $\nu_T^{(n)}$ and $\nu_B^{(n)}$, are adjusted depending on $\Delta \Theta^{(n)}$ and $\Delta \Gamma^{(n)}$, and at the final iterations take on values close to unity. Using this set of self-consistent criteria, the results can be shown, by explicit calculations, to be sensitive to change in the parameters, namely, γ and b , at least of the order $O(10^{-2})$ in the regions of the parameter space we will be investigating.

III. DOMAINS

It is well established that the boundary is strictly circular for a domain with a boojum texture when elastic anisotropy and line-tension anisotropy are not present, or $\gamma = b = 0$ [10]. This texture-boundary combination is indeed a local minimum of Eq. (2.1) [16]. Thus, in order for there to be noncircular domains, it is necessary to retain terms in the expansion Eq. (2.3) up to at least terms varying as a_2 . Using the numerical algorithm described above, we have performed systematic studies of the domain textures and shapes in terms of the elastic anisotropy and the line-tension anisotropy as well as the domain size. The quantity b defined earlier as $(K_s - K_b)/(K_s + K_b)$ parametrizes the elastic anisotropy. When $b > 0$, bend textures are preferred; splay is preferred when $b < 0$. The line-tension anisotropy is parametrized by $\gamma \equiv a_2/a_1$. The coefficient a_1 will be positive for convenience [12]. Then, the inequality $\gamma > 0$ corresponds to the case in which the \hat{c} directors on the boundary prefer to lie tangent to

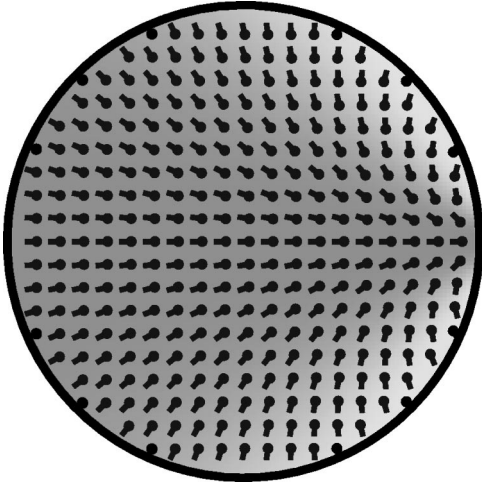


FIG. 3. Circular domain with a boojum texture, $R_0=5$, $\sigma_0=4$, $a_1=1.6$, $a_2=0$, $\kappa=1$, and $b=0$. Also shown in the background is the simulated image that would be obtained by Brewster angle microscopy.

it while $\gamma < 0$ applies when the \hat{c} directors prefer to point along the normal to the boundary, $\pm \hat{n}$. The variations of these anisotropic parameters are associated with the microscopic details of the Langmuir monolayers, such as the chain length of the surfactant molecules and the interactions between them. However, the correspondence between the anisotropic parameters and the microscopic details has not yet been fully established. Before we describe our observation, we note that, when $\gamma = b = 0$, the exact result is given by a circular boundary of radius R_0 together with a boojum texture with a $+2$ defect located a distance $R_B \equiv R_0(1 + \sqrt{1 + \rho_0^2})/\rho_0$ from the center of the domain, where $\rho_0 \equiv R_0 a_1 / \kappa$ is the normalized domain radius [10]. An exact equilibrium texture-boundary combination is shown in Fig. 3. The simulated image obtained using Brewster angle microscopy (BAM) is also displayed in the background. The signature of a boojum in a BAM image is a set of straight constant-intensity lines emerging from a virtual defect slightly outside the domain. The light intensity in a BAM image depends on the exact experimental setup and the properties of the monolayer [17]. In the case of all simulated BAM images presented in Fig. 3 and elsewhere in this report, the Brewster angle is taken to be that of water $\Theta_B = 53.12^\circ$, the angle of the analyzer α is equal to 90° , the thickness of the monolayer is assumed to be $d = 0.3$ nm, the tilt is 30° , the dielectric constants of the monolayer are $\epsilon_\perp = 2.31$, $\epsilon_\parallel = 2.43$, and it is assumed that the wavelength of the light $\lambda = 514$ nm.

We first concentrate on the effects of b and keep $\gamma = 0$. When $b < 0$, the texture is altered in such a way that the virtual defect appears to move closer to the boundary. This is observed as accelerated convergence of the constant-intensity lines to a point on the boundary. On the other hand, when $b > 0$, the texture relaxes as if the virtual defect has moved away from the boundary. The deviation of the texture from the boojum texture is as large as 20% when $|b| \approx 0.8$. The textural response is qualitatively in accord with that reported in Ref. [11]. Although there are significant textural corrections due to the presence of bulk elastic anisotropy, the

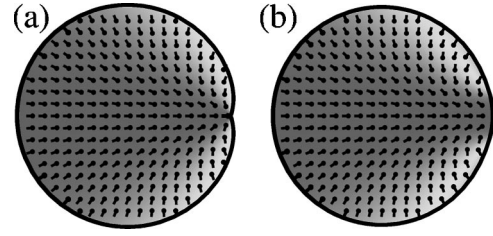


FIG. 4. The textures and shapes of domains with $R_0=5$, $\sigma_0=4$, $a_1=1.6$, and $a_2=0$. Their stiffness coefficients are (a) $\beta = -0.8$, (b) $\beta = 0.8$.

resultant textures very much resemble a boojum as seen in the BAM image shown in Fig. 4. This means that it is difficult to identify elastic anisotropy based on observation of the textures in the domains. The response of the boundary to elastic anisotropy that we obtain contrasts with that reported in Ref. [11]. The domain acquires an indentation when $b < 0$. The indentation remains observable for a large range of domain sizes. The boundary protrudes slightly for $b > 0$, as depicted in Fig. 4. The protrusion when $b = +0.8$ is subtle and does not resemble the sharp feature observed experimentally. Thus, elastic anisotropy alone is not capable of accounting for the shapes of the domains observed experimentally. Figure 5 shows domains of various sizes when (a) $b = -0.8$ and (b) $b = +0.8$.

We now proceed to discuss the role of the line-tension anisotropy, parametrized by γ , in the textures and boundaries of the domains. Elastic anisotropy will be eliminated ($b = 0$) for simplicity. We first investigate situations when $|\gamma| \leq 1$. For very small domains where $R_0 a_1 / \kappa \ll 1$, the texture is almost constant and the dominant contribution to the boundary deformation is the a_2 contribution. The domain is elongated at both ends along the axis connecting its center and the virtual defect when $\gamma > 0$, and is flattened at both ends along the same axis when $\gamma < 0$. Domain shapes exhibit a twofold symmetry. When $R_0 a_1 / \kappa \geq 1$, the texture closely resembles the boojum texture and contributes significantly to the boundary distortion through the influence of γ on the line tension. The domain no longer displays twofold symmetry and acquires a protrusion when $\gamma > 0$, or an indentation when $\gamma < 0$. Figure 6 shows domains with γ ranging from -0.5 to 0.5 . The numerical algorithm also allows us to examine domain shape and texture when $a_1 = 0$ and $a_2 = 1$. In this case, the domain acquires a ‘‘cigar shape’’ and the texture is associated with two virtual $+1$ defects [10,12]. The progressive changes of the texture and the shape from a system with

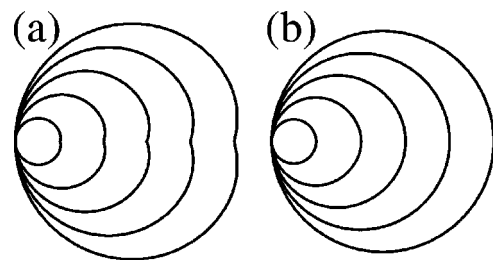


FIG. 5. The domain shapes computed for $a_0=4$, $a_1=1.6$, and $a_2=0$, and $R_0=0.5, 1, 2, 4, 8$. Their stiffness coefficients are (a) $\beta = -0.8$, (b) $\beta = 0.8$. For ease of observation, domains are not shown to scale.

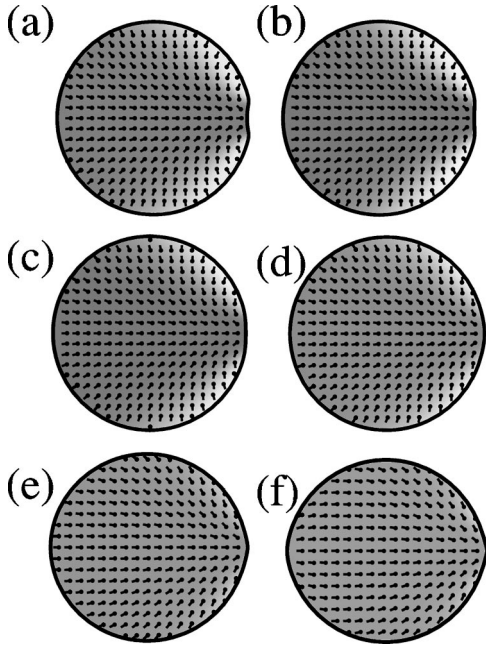


FIG. 6. The textures and shapes of domains computed for $-0.5 < a_2 < 0.5$, $R_0 = 5$, $\sigma_0 = 4$, $a_1 = 1$. (a) $a_2 = -0.5$, (b) $a_2 = -0.3$, (c) $a_2 = -0.1$, (d) $a_2 = 0.1$, (e) $a_2 = 0.3$, and (f) $a_2 = 0.5$.

$a_1 = 1$ and $a_2 = 0$ to one for which $a_1 = 0$ and $a_2 = 1$ are shown in Fig. 7. When both a_1 and a_2 are nonzero, the texture can be thought of as a superposition of pure a_1 and pure a_2 textures. Typically, at $R_0 a_1 / \kappa \sim 1$, the effect of the set of two $+1$ defects becomes observable when $\gamma = 1/4$. Domains with indentation and protrusions and the cigar-shaped domains, have all been observed experimentally [18].

We have already briefly discussed the issue of size dependence in the previous paragraph. To look into this matter in detail, we will examine the particular set of data reported in

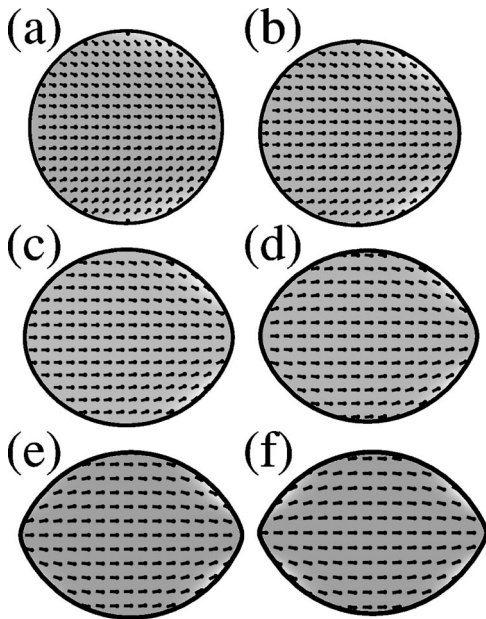


FIG. 7. The textures and shapes of domains with $\rho = 1$ and $a_0 = 4$. Their coefficients of the anisotropy line tension are (a) $a_1 = 1$, $a_2 = 0$, (b) $a_1 = 0.8$, $a_2 = 0.2$, (c) $a_1 = 0.6$, $a_2 = 0.4$, (d) $a_1 = 0.4$, $a_2 = 0.6$, (e) $a_1 = 0.2$, $a_2 = 0.8$ and (f) $a_1 = 0$, $a_2 = 1$.

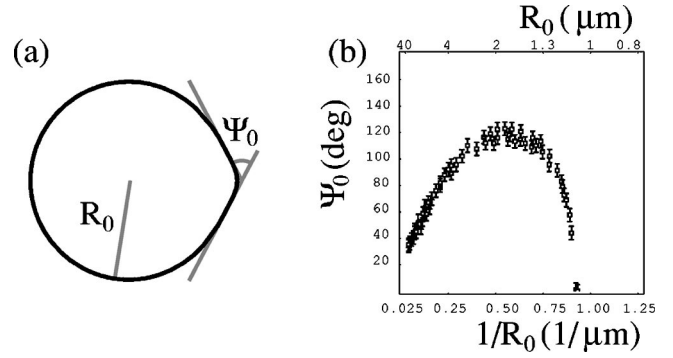


FIG. 8. (a) The definition of the excluded angle Ψ_0 . (b) Experimental measurements of the domain-size R_0 dependence of Ψ_0 observed in the domains of the L_2 phase (one of the tilted phases) surrounded by the L_1 phase (one of the isotropic phases) taken from Ref. [7].

Ref. [7], in which the domains investigated possess protruding features sharp enough that “excluded angles” Ψ_0 characterizing the boundaries can be identified. The definition of Ψ_0 and the experimental data are depicted in Fig. 8. The key features of this set of experimental data are that (1) Ψ_0 goes through a maximum as R_0 varies; (2) there is an abrupt onset of Ψ_0 in the small R_0 region; and (3) the intercept at the Ψ_0 axis when the curve is extrapolated implies $\lim_{R_0 \rightarrow \infty} \Psi_0 \neq 0$.

Before we make comparisons between theoretical results and the experimental data, we comment on the extraction of Ψ_0 from computed domain boundaries. It has been shown that, within the parameter regime of our discussions, the domain boundaries are smooth and continuous. There is no cusplike singularity on the boundary. This can be seen in the domains of various sizes shown in Fig. 9. Nevertheless, Ψ_0 can be unambiguously measured for some of these domains. The values of the parameters utilized here are $\kappa = 1$, $\delta = 0.4$, and $\gamma = 0.5$. To determine Ψ_0 for these domains, we adopt a systematic scheme (devised in Ref. [12]) that utilizes the function $I \equiv I_0 \exp[-(d^2x/dy^2)^2]$ to capture the most likely Ψ_0 for a given domain bounding curve, where $x(y)$ parametrizes Γ in a Cartesian coordinates system. Density plots of I as a function of $\Psi \equiv -2 \tan^{-1} dx/dy$ and R_0 for numerical and the perturbative results are shown, respectively, in Figs. 10(a) and 10(c), the darker regions representing larger I , and highlighting the more likely values of Ψ_0 . With the use of this method for the determination of Ψ_0 , we have obtained reasonable agreement between the perturba-

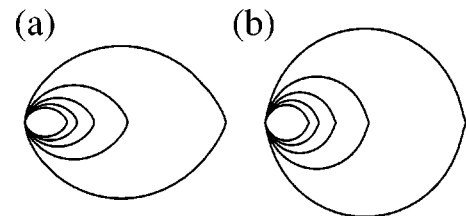


FIG. 9. The shapes of domains of various sizes computed for $\sigma_0 = 4$, $a_1 = 1.6$, and $a_2 = 0.8$. (a) Smaller domains with $R_0 = 0.2, 0.25, 0.33, 0.5$, and 1 , which exhibit two-fold symmetry. (b) Larger domains with $R_0 = 2, 2.5, 3.3, 5$, and 10 , which have a protrusion on one end of the boundary. Each of the sets of domains is plotted to scale.

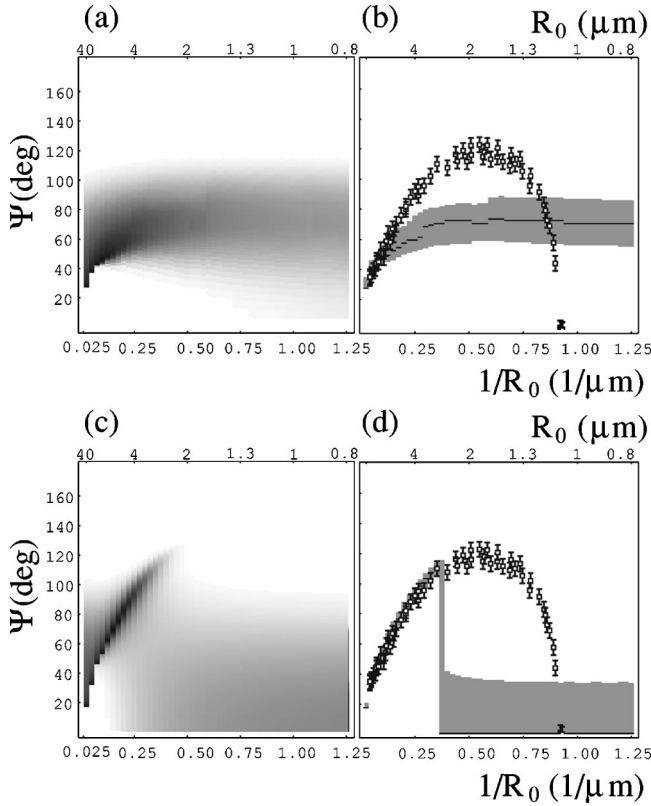


FIG. 10. (a) Density plot of I as a function of Ψ and R_0 of the numerical results for the domains. (b) Plot of I_{max} and the region in which $I > I_{max}/2$ as a function of Ψ and R_0 of the numerical results for the domains. Superimposed are the experimental data shown in Fig. 8(b) with parameters $\kappa/a_1 = 4 \mu\text{m}$, $\delta = 0.4$, and $\gamma = 0.5$. (c) and (d) are corresponding plots for the perturbative results.

tive analysis and the numerical computations in the large- R_0 regime. We note here that the value at which γ is set, 0.5, is too large for perturbative results to be dependable. However, the perturbative results resemble those obtained numerically in the sense that Ψ_0 increases as R_0 decreases from ∞ . The abrupt onset of Ψ_0 indicated in Figs. 10(c) and 10(d) is not present in Figs. 10(a) and 10(b). It is, however, evident in Figs. 9 that Ψ_0 can be unambiguously identified for domains with $R_0 \geq 1$. When $R_0 < 1$, the domains become elliptical and $\Psi_0 = 0$. Hence, there is an apparent jump in Ψ_0 near $R_0 = 1$, beyond which Ψ_0 becomes nonzero. The jump in Ψ_0 predicted in the perturbative analysis [12] is indeed confirmed by the more reliable numerical computations reported here. For very small domains ($R_0 < 1$), the shapes are predicted to be elliptical by our numerical analysis, in contrast to the prediction of nearly circular domains that results from the perturbative analysis. The magnitude of γ that results in breakdown of the first-order perturbative analysis is the key origin of the mismatch. In Figs. 10(b) and 10(d), the maximum I_{max} of I is shown as the dark line segments and the gray bands mark the regions in which $I > I_{max}/2$. They depict, respectively, numerical and perturbative results. Superimposed are the experimental data, which provide a reference for the comparisons described above.

To compare the theoretical results to the experimental data, a length scale is required. The length scale is set by the assignment $\kappa/a_1 = 4 \mu\text{m}$ when the comparison is made be-

tween the perturbative results and the experimental data [12]. Except for examining the results of more reliable computations, there is no attempt to fit the experimental data in this report for reasons to be discussed below. We first adopt the same set of parameters with which the perturbative analysis fits the data in the large- R_0 regime, for the comparison. It is obvious from Fig. 10(b) that even at $\gamma = 0.5$, the theoretical prediction for the maximum of Ψ_0 is much smaller than that observed experimentally. This superficial comparison between the maxima of Ψ_0 implies that γ is very much larger in the system investigated. Detailed comparisons do show excellent agreement for domains larger than $10 \mu\text{m}$. Experimentally observed domains with maximum Ψ_0 and small circular domains are not reproduced numerically. Attempts have been made to investigate the combined effect of the elastic anisotropy b and γ . However, for γ of such a magnitude, contributions from b do not affect the qualitative behaviors discussed in this context. It is thus concluded that, although the simple elastic model is not capable of fully addressing the issue of the domain size dependence of the shapes, it has successfully produced the qualitative features in the Ψ_0 versus R_0 plot and many nontrivial domain shapes observed in various experiments [18].

In the large- R_0 regime ($R_0 \gg 1$), the boundary corrections are confined in a small portion of the boundary and the domains become nearly circular. Because of the rapid texture variations in the immediate vicinity of the boundary, associated with the approach to the boundary of the virtual defect, we are unable to perform dependable numerical investigations of extremely large domains. This leaves open the question of the asymptotic behavior of Ψ_0 in the $R_0 \rightarrow \infty$ limit.

With the numerical scheme for evaluating Θ and Γ simultaneously, we are able to explore the simple model Eq. (2.1) in a much wider range of the parameter space with confidence. Not only does the model account for domains with various features observed in experiments, it also yields an appropriate domain size dependence of the boundary shapes. However, we are unable to perform reliable numerical investigations on extremely large domains. Despite the fact that there is an upper bound to the domain size that we are able to compute, we believe, on the basis of measurements of the defect positions [5], that the largest domains we are able to compute are not smaller than those that have been observed experimentally. The numerical algorithm appears to be capable of evaluating domain shapes for arbitrary anisotropic line tension, with one caveat. A closer look at Eqs. (2.13) and (2.14) immediately indicates that this approach is not appropriate for situations in which $\sigma + \sigma'' = 0$ at some points on the boundary. An approach that is appropriate to this situation is the Wulff construction [10].

IV. BUBBLES

We now turn to the investigation of bubbles. The first task is to numerically evaluate the texture in a region Ω that does not have an external boundary. It is possible to implement a straightforward extension of the problem of the domain by introducing an artificial external boundary far away from the inner bounding curve Γ . One must introduce a boundary condition on this added external boundary by hand. Figure 11 displays the triangulations associated with such an imple-

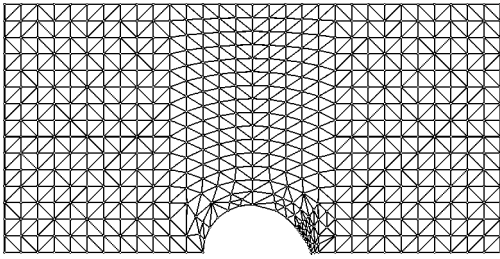


FIG. 11. Mesh with additional external boundary used in the direct extension of the FEM algorithm for bubbles.

mentation of the approach to the calculation of the property of a bubble. The method, though inefficient, produces results that are consistent with those obtained perturbatively [12].

The problem that involves an *infinite* Ω with internal boundary Γ is referred to as the exterior problem. If one does not introduce an artificial external boundary, it is necessary to have at hand a complete set of exterior solutions to construct the boundary condition at Γ . For our particular case, this is possible when $b=0$, in which case the bulk extremum equation reduces to Laplace’s equation. The examination of the problem with nonzero b is a major goal of this investigation, and we are not aware of the existence of an appropriate set of external solutions in this case. Noting that the order parameter tends to a fixed value ($\Theta=0$ for our case here) as $r\rightarrow\infty$, it is possible to approach the problem of the bubble using a different set of polar coordinates, i.e., $(r',\varphi)\equiv(1/r,\varphi)$, that transform the bubble into a domain of area Ω' and bounding curve Γ' , shown in Fig. 12, with the “elastic energy”

$$\mathcal{H} = \frac{\kappa}{2} \int_{\Omega'} \{ \Theta_x^2 + \Theta_y^2 + \beta [(-\Theta_x^2 + \Theta_y^2) \cos 2(\Theta - 2\varphi) + 2\Theta_x\Theta_y \sin 2(\Theta - 2\varphi)] \} dA + \oint_{\Gamma'} \frac{\sigma(\vartheta - \Theta)}{R^{-2}} ds.$$

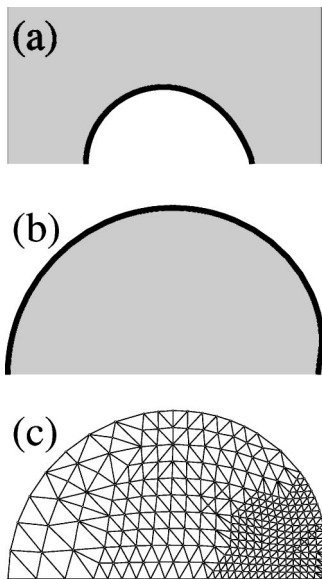


FIG. 12. Solving the problem of the bubble by transforming it into an inverse domain problem. (a) shows the region Ω of ordered phase and the boundary Γ for the bubble. (b) shows the transformed region Ω' and boundary Γ' . (c) shows the mesh that covers Ω' .

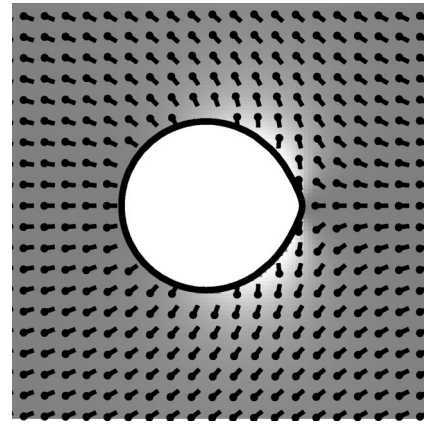


FIG. 13. Boundaries and textures around the bubbles for $R_0=5$, $a_1=1$, $\kappa=1$, and $b=0$.

With the problem transformed, the meshing algorithm used for the domain can be applied immediately. We are then able to proceed with the investigation of the bubbles with the same efficiency and accuracy as in the studies of the domains.

In the numerical studies that we have performed with the use of the transformation above, the results for the bubbles reported in the perturbative analysis [12,7], that the boundaries are not circular even when $b=0$ and $a_2=0$, have been confirmed. Figure 13 shows the texture and the boundary of a typical bubble. In the background simulated BAM image, one notes the circular constant-intensity lines that identify the “inverse boojum.” The numerical algorithm further enables us to obtain equilibrium bubble boundaries and textures around them when elastic anisotropies are present. As can be seen in Fig. 14, the elastic anisotropy leaves the boundaries substantially unaffected while significantly changing the appearance of the textures around the bubbles. The BAM images are also shown in the same figures. In contrast to the case in which $b=0$, the constant-intensity lines become elongated perpendicular to the axis connecting the center of the bubble and the position of the virtual defect when $b<0$. These lines are elongated in the direction of the axis when $b>0$, as shown. This allows for the determination of the sign of b in the Langmuir monolayer by examining the BAM images of the bubbles.

In Figs. 15, we display the size dependence of the bubble boundaries. Bubbles appear to be circular when they are small ($R_0<1$). For large enough bubbles ($R_0\geq 1$), an “excluded angle” Ψ_0 defined in Fig. 8(a) can be identified. An approach similar to the analysis of the size dependence of the

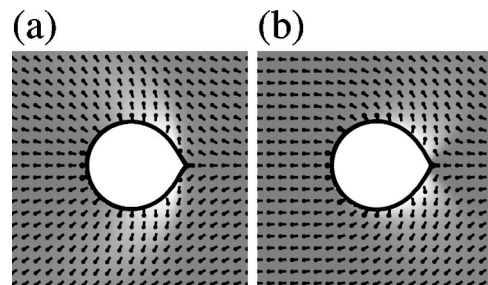


FIG. 14. Boundaries and textures around the bubbles for $R_0=5$, $a_1=1$, $\kappa=1$, (a) with $b=-0.8$ and (b) with $b=0.8$.

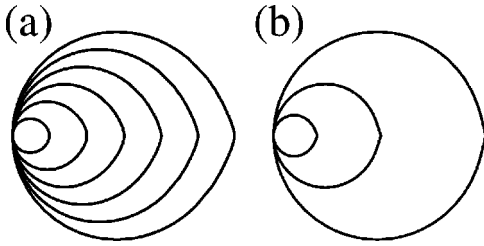


FIG. 15. Boundaries of bubbles computed for $\kappa=0.16$, $\sigma_0=1$, $a_1=0.16$ and (a) $R_0=1,2,3,4,5,6$, and (b) $R_0=8,20,40$.

boundary in the case of domains can be applied. Figures 16(a) and 16(c) compare the density plots of I as a function of Ψ versus R_0 for the numerical and the perturbative results. The two plots are in excellent agreement. When $\gamma=0$, the texture does not differ significantly from that of the inverse boojum even though the bubble is not exactly circular. This contrasts with what is seen in domains when $\gamma \neq 0$, in which case the textures can deviate significantly from the boojum texture. The R_0 dependence of Ψ_0 has features that are qualitatively similar to those seen in the case of domains, i.e., a maximum and an onset. These features have also been observed experimentally [7]. Experimental data are shown together with the numerical and perturbative results in Figs. 16(b) and 16(d), respectively, and all the results match rea-

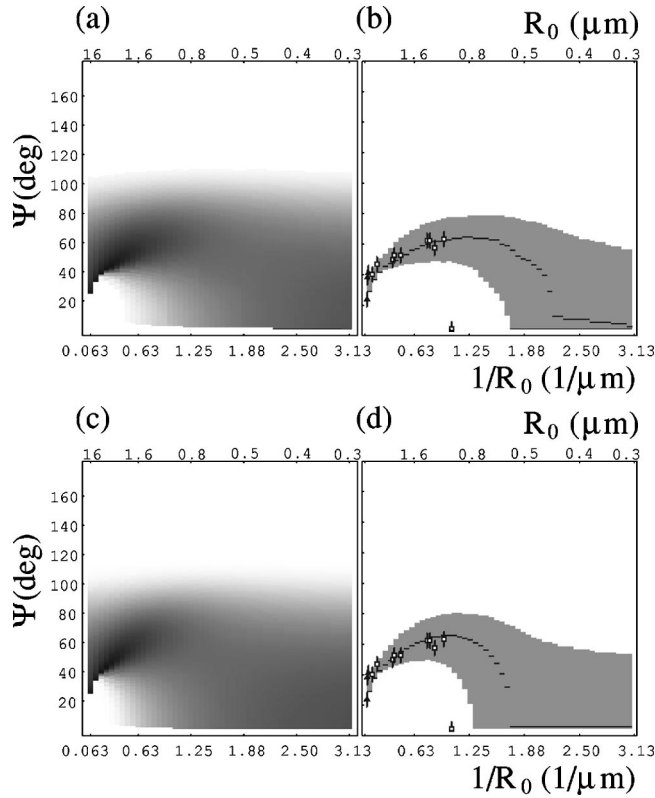


FIG. 16. (a) Plot of I as a function of Ψ and R_0 of the numerical results for the bubbles. (b) Plot of I_{max} and the region in which $I > I_{max}/2$ as a function of Ψ and R_0 of the numerical results for the bubbles. Superimposed are the experimental observations of gaseous bubbles in the L_2 phase. The experimental data have appeared in Ref. [7]. The parameters for the by-eye fit are $\kappa/a_1=0.4 \mu\text{m}$ and $\delta=0.16$. (c) and (d) are the corresponding plots for the perturbative results.

sonably well. The by-eye fit was obtained in Ref. [7] and no further adjustment of the parameters is made in this investigation.

We have thus devised a numerical method to approach the problem of the bubble that can be implemented with the same efficiency as in the problem of the domain. There is good agreement between perturbative and numerical results. We are able to investigate the effect of the elastic anisotropy, and our results point to a possible means for the determination of the relative strength of K_s and K_b .

V. CONCLUSIONS

We have discussed in this report the implementation of a numerical method that leads us to the solution of simultaneous equilibrium conditions for the textures and the bounding curve of the domains. Using this numerical algorithm, we have investigated the influences on the textures and domain shapes of the line-tension and elastic anisotropies. Our analysis of this simple model reveals that elastic anisotropy does, indeed, result in interesting domain boundaries with protrusions and indentations. The domains with indentations resemble those observed experimentally. However, the domains that we generate with protrusions are very different from those in observed in BAM images [18]. Hence, elastic anisotropy cannot qualitatively account for all experimental observations. Furthermore, our numerical results are in contrast to the claims in Ref. [11]. Dents in boundaries are due to a bend modulus that exceeds the splay modulus, i.e., $b \equiv (K_s - K_b)/(K_s + K_b) < 0$, while protrusions are present when $b > 0$. On the other hand, the second harmonic contribution to the line tension, parametrized by $\gamma \equiv a_2/a_1$, is capable of producing nontrivial domain shapes that resemble the shapes observed experimentally. For the influence of γ on the boundary, our results are in qualitative agreement with those presented in Ref. [11]. Comparison has also been made between perturbative results [12], the numerical computations described here, and the experimental data [7]. The magnitude of γ used in the perturbative analysis is the prime factor causing the mismatch between the perturbative and numerical results. When γ is large ($=0.5$ for our case), the first-order perturbative approach is not expected to be accurate.

While the results of the perturbative analysis and the numerical study are different quantitatively, they possess similar qualitative features, namely, the onset of the excluded angle Ψ_0 as the domain size R_0 increases, followed by Ψ_0 reaching a maximum and then decreasing as R_0 continues to increase. These match the qualitative features that are present in the experimental data [7] shown in Fig. 8(b). Experimental results are not reproduced in the numerical calculations when R_0 is small. The discrepancies between the experimental data and the numerical result imply that other interactions, neglected in the model, may be significant.

We have also extended the numerical algorithm to the problem of bubbles. It is found that the transformation $r \rightarrow r' \equiv 1/r$ results in a new domain problem which allows us to solve the equilibrium conditions for the bubbles at the same level of efficiency and accuracy as those for the domains. Not only have we obtained results that are consistent with those in the perturbative analysis [7,12], we have also

analyzed the effect of elastic anisotropy on the textures and the boundary of the bubbles, a task that is algebraically formidable in a perturbative analysis. The influence of elastic anisotropy on the boundary is small while it significantly modifies the textures. This provides a means for the qualitative determination of the elastic anisotropy by observing the texture around the bubbles. The agreement between the perturbative results and the numerical computation is excellent. This is not surprising as a_2 is not involved. The R_0 dependence of Ψ_0 is similar to that in the case of the domain, except that the maximum of Ψ_0 is much smaller. The perturbative result agrees reasonably well with the experimental data as reported in Ref. [7]. The numerical results match as well.

In conclusion, we have successfully implemented a numerical algorithm that enables us to analyze unambiguously a simple model, Eq. (2.1), of tilted ordered media in a non-trivial geometry imposed by experimental observations. Using this numerical algorithm and its extensions, we are able to address the long-standing debate with regard to the origin of the cusplike features observed in domains of Langmuir monolayers using an elastic model. Within the context of this simple model, which addresses only the competition between the bulk elastic energy and the boundary energy, many qualitative features of the experimental observations have been captured. Discrepancies cannot be avoided, as the real system is much more complex. The model we adopted has neglected other effects and interactions that are present in the real system, such as dipolar interactions and adjustments in the tilt degree of freedom. A combination of these effects may account for the discrepancies between the experimental data and the theoretical results. The apparently general numerical algorithm is, however, not capable of handling situations in which $\sigma + \sigma'' = 0$ at some points on the boundary. A different approach, such as the Wulff construction [10], is required. Nevertheless, our numerical algorithm is versatile and can be extended to systems containing topological defects, or with the ordered phase filled in a non-simply-connected space.

ACKNOWLEDGMENTS

We thank Professor Charles Knobler, Professor Robijn Bruinsma, Dr. Jiyu Fang, and Ellis Teer for useful discussions. We are grateful to Professor Robert Meyer for his insightful proposal of the compact and concise way of presenting the textures.

APPENDIX A: VARIATIONAL FORMULATION OF THE FEM

In finite element analysis, we approximate $\Theta(x, y)$ by Eq. (2.7). The energy functional $H[\Theta]$ given in Eq. (2.1) now becomes

$$H(\Theta) = \frac{\kappa}{2} \int_{\Omega} \{ |\nabla \Theta|^2 + b[(-\Theta_x^2 + \Theta_y^2) \cos 2\Theta - 2\Theta_x \Theta_y \sin 2\Theta] \} dA + \oint_{\Gamma} \sigma(\vartheta - \Theta) ds, \quad (A1)$$

where we put $\Theta \equiv (\Theta_1, \Theta_2, \dots, \Theta_N)^T$, and $\Theta = \sum \varphi_i \Theta_i$. We differentiate Eq. (A1) with respect to Θ_i yielding

$$\begin{aligned} \frac{\partial H(\Theta)}{\partial \Theta_i} = & \kappa \int_{\Omega} [\varphi_{ix} \varphi_{jx} (1 - b \cos 2\Theta) \\ & + \varphi_{iy} \varphi_{jy} (1 + b \cos 2\Theta) \\ & + b(\varphi_{ix} \varphi_{jy} + \varphi_{iy} \varphi_{jx}) \sin 2\Theta] dA \Theta_j \\ & - \kappa b \int_{\Omega} [(-\Theta_x^2 + \Theta_y^2) \sin 2\Theta \\ & + 2\Theta_x \Theta_y \cos 2\Theta] \varphi_i dA \\ & - \oint_{\Gamma} \sigma'(\vartheta - \Theta) \varphi_i ds. \end{aligned} \quad (A2)$$

The equilibrium condition gives $\mathbf{A}\Theta = \mathbf{b}$ with \mathbf{A} and \mathbf{b} provided in Eqs. (2.10) and (2.11).

APPENDIX B: INTEGRATION OVER A TRIANGULATION

The integrals in Eqs. (2.10) and (2.11) over Ω are broken up into sums of integration over the triangles in the triangulation of Ω . Integration over the interior individual triangles can usually be carried out analytically, depending on the specific forms of the basis functions $\varphi_i(x, y)$ and the matrix elements A_{ij} and b_i . We have chosen $\varphi_i(x, y)$ to be a continuous, piecewise linear function in x and y within a triangle. The line integral $\oint_{\Gamma} ds$ in b_i must be evaluated numerically, because the integrand depends on the polar angle φ , which is not linear in x or y . This does not degrade the efficiency of the computation because, first of all, only triangles whose perimeters coincide with Γ contribute to the line integral, and secondly it is a line integral over a short distance.

In Eq. (2.7), we express the function $f(x, y)$ for $(x, y) \in \Omega$ in terms of its values at the nodes of the triangulation and the corresponding basis functions $\varphi_i(x, y)$. Within an individual triangle K , we can write

$$f(x, y) = \sum_{i=1}^3 f_{K_i} \varphi_{K_i}^{(K)}(x, y), \quad (B1)$$

where K_i is the index of the i th vertex of the triangle K , and $f_{K_i} = f(x_{K_i}, y_{K_i})$ and (x_{K_i}, y_{K_i}) are, respectively, the functional value of $f(x, y)$ and the coordinates of the i th vertex. $\varphi_{K_i}^{(K)}(x, y)$ is the restriction of $\varphi_{K_i}(x, y)$ in K . The actual index of the i th vertex is K_i . It is, however, awkward to carry the K in the symbol K_i throughout the discussion. We will use i to identify the vertex for simplicity from now on, i.e., f_{K_i} is simplified as f_i . We introduce a set of natural coordinates u and v such that

$$f(u, v) = f_1 + (f_2 - f_1)u + (f_3 - f_1)v, \quad (B2)$$

where $u \in [0, 1]$, $v \in [0, 1]$, and $u + v \leq 1$. Transformation between variable sets $x - y$ and $u - v$ can be obtained from Eq. (B2) by substituting f with x and y . We then have the following relations:

$$u = \frac{1}{\Delta} [(y_3 - y_1)x - (x_3 - x_1)y + x_3y_1 - x_1y_3], \quad (\text{B3})$$

$$v = \frac{1}{\Delta} [(y_1 - y_2)x - (x_1 - x_2)y + x_1y_2 - x_2y_1], \quad (\text{B4})$$

where Δ is the Jacobian determinant given by

$$\Delta = \frac{\partial(x, y)}{\partial(u, v)} = x_1y_2 - y_1x_2 + x_2y_3 - x_3y_2 + x_3y_1 - x_1y_3. \quad (\text{B5})$$

Identifying Eqs. (B1) and (B2), we find $\varphi_1(u, v) = 1 - u - v$, $\varphi_2(u, v) = u$ and $\varphi_3(u, v) = v$. In terms of $x - y$, we have

$$\varphi_1(x, y) = \frac{1}{\Delta} [(y_2 - y_3)x - (x_2 - x_3)y + x_2y_3 - x_3y_2], \quad (\text{B6})$$

$$\varphi_2(x, y) = \frac{1}{\Delta} [(y_3 - y_1)x - (x_3 - x_1)y + x_3y_1 - x_1y_3], \quad (\text{B7})$$

$$\varphi_3(x, y) = \frac{1}{\Delta} [(y_1 - y_2)x - (x_1 - x_2)y + x_1y_2 - x_2y_1]. \quad (\text{B8})$$

Evaluation of the matrix element A_{ij} involves the following area integrals, which can be computed analytically. The trivial one is the area of K , which is $\int_K dA = |\Delta|/2$, and

$$\int_K \cos 2\Theta \, dA = \frac{|\Delta|}{4} \left(\frac{\cos 2\Theta_1}{(\Theta_1 - \Theta_2)(\Theta_2 - \Theta_3)} + \frac{\cos 2\Theta_2}{(\Theta_2 - \Theta_3)(\Theta_3 - \Theta_1)} + \frac{\cos 2\Theta_3}{(\Theta_3 - \Theta_1)(\Theta_1 - \Theta_2)} \right), \quad (\text{B9})$$

$$\int_K \sin 2\Theta \, dA = \frac{|\Delta|}{4} \left(\frac{\sin 2\Theta_1}{(\Theta_1 - \Theta_2)(\Theta_2 - \Theta_3)} + \frac{\sin 2\Theta_2}{(\Theta_2 - \Theta_3)(\Theta_3 - \Theta_1)} + \frac{\sin 2\Theta_3}{(\Theta_3 - \Theta_1)(\Theta_1 - \Theta_2)} \right), \quad (\text{B10})$$

as φ_{ix} and φ_{iy} are constants. Evaluation of b_i involves

$$\int_K \varphi_1 \cos 2\Theta \, dA = \frac{|\Delta|}{4} \left(\frac{\cos 2\Theta_1}{(\Theta_3 - \Theta_1)(\Theta_1 - \Theta_2)} + \frac{\sin 2\Theta_1 - \sin 2\Theta_3}{2(\Theta_1 - \Theta_3)^2(\Theta_3 - \Theta_2)} - \frac{\sin 2\Theta_1 - \sin 2\Theta_2}{2(\Theta_1 - \Theta_2)^2(\Theta_3 - \Theta_2)} \right), \quad (\text{B11})$$

$$\int_K \varphi_2 \cos 2\Theta \, dA = \frac{|\Delta|}{4} \left(\frac{\cos 2\Theta_2}{(\Theta_1 - \Theta_2)(\Theta_2 - \Theta_3)} + \frac{\sin 2\Theta_2 - \sin 2\Theta_3}{2(\Theta_2 - \Theta_3)^2(\Theta_3 - \Theta_1)} - \frac{\sin 2\Theta_2 - \sin 2\Theta_1}{2(\Theta_1 - \Theta_2)^2(\Theta_3 - \Theta_1)} \right), \quad (\text{B12})$$

$$\int_K \varphi_3 \cos 2\Theta \, dA = \frac{|\Delta|}{4} \left(\frac{\cos 2\Theta_3}{(\Theta_2 - \Theta_3)(\Theta_3 - \Theta_1)} + \frac{\sin 2\Theta_3 - \sin 2\Theta_2}{2(\Theta_2 - \Theta_3)^2(\Theta_2 - \Theta_1)} - \frac{\sin 2\Theta_3 - \sin 2\Theta_1}{2(\Theta_1 - \Theta_3)^2(\Theta_3 - \Theta_1)} \right), \quad (\text{B13})$$

$$\int_K \varphi_1 \sin 2\Theta \, dA = \frac{|\Delta|}{4} \left(\frac{\sin 2\Theta_1}{(\Theta_3 - \Theta_1)(\Theta_1 - \Theta_2)} - \frac{\cos 2\Theta_1 - \cos 2\Theta_3}{2(\Theta_1 - \Theta_3)^2(\Theta_3 - \Theta_2)} + \frac{\cos 2\Theta_1 - \cos 2\Theta_2}{2(\Theta_1 - \Theta_2)^2(\Theta_3 - \Theta_2)} \right), \quad (\text{B14})$$

$$\int_K \varphi_2 \sin 2\Theta \, dA = \frac{|\Delta|}{4} \left(\frac{\sin 2\Theta_2}{(\Theta_1 - \Theta_2)(\Theta_2 - \Theta_3)} - \frac{\cos 2\Theta_2 - \cos 2\Theta_3}{2(\Theta_2 - \Theta_3)^2(\Theta_3 - \Theta_1)} + \frac{\cos 2\Theta_2 - \cos 2\Theta_1}{2(\Theta_1 - \Theta_2)^2(\Theta_3 - \Theta_1)} \right), \quad (\text{B15})$$

$$\int_K \varphi_3 \sin 2\Theta \, dA = \frac{|\Delta|}{4} \left(\frac{\sin 2\Theta_3}{(\Theta_2 - \Theta_3)(\Theta_3 - \Theta_1)} - \frac{\cos 2\Theta_3 - \cos 2\Theta_2}{2(\Theta_2 - \Theta_3)^2(\Theta_2 - \Theta_1)} + \frac{\cos 2\Theta_3 - \cos 2\Theta_1}{2(\Theta_1 - \Theta_3)^2(\Theta_3 - \Theta_1)} \right). \quad (\text{B16})$$

The above formulas will work only if $\Theta_1 \neq \Theta_2 \neq \Theta_3$. Let us consider cases where the values of $\Theta = \Theta_E$ at two vertices of triangle K and $\Theta = \Theta_O$ at the other vertex. We obtain the following for the integrals in A_{ij} :

$$\int_K \cos 2\Theta \, dA = \frac{|\Delta|}{4} \left(\frac{\cos 2\Theta_E - \cos 2\Theta_O}{(\Theta_E - \Theta_O)^2} + \frac{2\sin 2\Theta_E}{\Theta_E - \Theta_O} \right), \quad (\text{B17})$$

$$\int_K \sin 2\Theta \, dA = \frac{|\Delta|}{4} \left(\frac{\sin 2\Theta_E - \sin 2\Theta_O}{(\Theta_E - \Theta_O)^2} - \frac{2\cos 2\Theta_E}{\Theta_E - \Theta_O} \right). \quad (\text{B18})$$

We denote as φ_E the restrictions of the basis functions at the nodes that have $\Theta = \Theta_E$, and as φ_O the restriction of the basis function at the node that has $\Theta = \Theta_O$. We arrive at

$$\int_K \varphi_E \cos 2\Theta \, dA = \frac{|\Delta|}{4} \left(\frac{\sin 2\Theta_E}{\Theta_E - \Theta_O} + \frac{\cos 2\Theta_E}{(\Theta_E - \Theta_O)^2} - \frac{\sin 2\Theta_E - \sin 2\Theta_O}{2(\Theta_E - \Theta_O)^3} \right), \quad (\text{B19})$$

$$\int_K \varphi_O \cos 2\Theta \, dA = \frac{|\Delta|}{4} \left(-\frac{\cos 2\Theta_E + \cos 2\Theta_O}{(\Theta_E - \Theta_O)^2} + \frac{\sin 2\Theta_E - \sin 2\Theta_O}{(\Theta_E - \Theta_O)^3} \right), \quad (\text{B20})$$

$$\int_K \varphi_E \sin 2\Theta \, dA = \frac{|\Delta|}{4} \left(-\frac{\cos 2\Theta_E}{\Theta_E - \Theta_O} + \frac{\sin 2\Theta_E}{(\Theta_E - \Theta_O)^2} + \frac{\cos 2\Theta_E - \cos 2\Theta_O}{2(\Theta_E - \Theta_O)^3} \right), \quad (\text{B21})$$

$$\int_K \varphi_O \sin 2\Theta \, dA = \frac{|\Delta|}{4} \left(-\frac{\sin 2\Theta_E + \sin 2\Theta_O}{(\Theta_E - \Theta_O)^2} - \frac{\cos 2\Theta_E - \cos 2\Theta_O}{(\Theta_E - \Theta_O)^3} \right) \quad (\text{B22})$$

for the integrals required to evaluate b_i . Finally, when $\Theta_i = \Theta_E$ for all i 's, one will need $\int_K \varphi_E \, dA = |\Delta|/6$.

APPENDIX C: DERIVATIVES ON THE BOUNDARY

One of the biggest benefits of the FEM is that it enables straightforward determination of the derivatives of Θ on the boundary. The tangential derivative at node i is

$$\frac{\partial \Theta}{\partial t} \Big|_i = \frac{1}{2e^k \sqrt{1+k^2}} \left(\frac{\Theta_{i+1} - \Theta_i}{\varphi_{i+1} - \varphi_i} + \frac{\Theta_i - \Theta_{i-1}}{\varphi_i - \varphi_{i-1}} \right). \quad (\text{C1})$$

The normal derivative of Θ is given by Eq. (2.5), which reads

$$\frac{\partial \Theta}{\partial n} = \frac{e^k \sigma'(\vartheta - \Theta) + \kappa b \Theta_i \sin 2(\Theta - \vartheta)}{\kappa [1 - b \cos 2(\Theta - \vartheta)]}. \quad (\text{C2})$$

-
- [1] C.M. Knobler and R.C. Desai, *Annu. Rev. Phys. Chem.* **43**, 207 (1992).
[2] J. Ruiz-Garcia, X. Qiu, M.-W. Tsao, G. Marshall, C.M. Knobler, G. A. Overbeck, and D. Möbius, *J. Phys. Chem.* **97**, 6955 (1993); D.K. Schwartz, J. Ruiz-Garcia, X. Qiu, J.V. Selinger, and C.M. Knobler, *Physica A* **204**, 606 (1994); J.V. Selinger, Z.-G. Wang, R.F. Bruinsma, and C.M. Knobler, *Phys. Rev. Lett.* **70**, 1139 (1993).
[3] X. Qiu, J. Ruiz-Garcia, K.J. Stine, C.M. Knobler, and J.V. Selinger, *Phys. Rev. Lett.* **67**, 703 (1991).
[4] T.M. Fischer, R.F. Bruinsma, and C.M. Knobler, *Phys. Rev. E* **50**, 413 (1994).
[5] S. Rivière and J. Meunier, *Phys. Rev. Lett.* **74**, 2495 (1995).
[6] N.D. Mermin, in *Quantum Fluids and Solids*, edited by S.B. Trickey, E. Adams, and J. Duffy (Plenum, New York, 1977).
[7] J. Fang, E. Teer, C.M. Knobler, K.-K. Loh, and J. Rudnick, *Phys. Rev. E* **56**, 1859 (1997).
[8] S.A. Langer and J.P. Sethna, *Phys. Rev. A* **34**, 5035 (1986).
[9] I. Kraus and R.B. Meyer, *Phys. Rev. Lett.* **81**, 3815 (1999).
[10] J. Rudnick and R. Bruinsma, *Phys. Rev. Lett.* **74**, 2491 (1995).
[11] P. Galatola and J.B. Fournier, *Phys. Rev. Lett.* **75**, 3297 (1995).
[12] J. Rudnick and K.-K. Loh, *Phys. Rev. E* **60**, 3045 (1999).
[13] C. Johnson, *Numerical Solution of Partial Differential Equations by the Finite Element Method* (Cambridge University Press, Cambridge, England, 1987).
[14] W.H. Press, B.P. Flannery, S.A. Teukolsky, and W.T. Vetterling, *Numerical Recipes in C: The Art of Scientific Computing* (Cambridge University Press, Cambridge, England, 1991).
[15] K.-K. Loh and J. Rudnick, *Phys. Rev. Lett.* **81**, 4935 (1998).
[16] D. Petley and T.C. Lubensky, *Phys. Rev. E* **59**, 1834 (1999).
[17] E. Teer and C.M. Knobler (private communications); C. Lautz, T.M. Fischer, M. Weygand, M. Lösche, P.B. Howes, and K. Kjaer, *J. Chem. Phys.* **108**, 4640 (1998).
[18] J. Fang and C.M. Knobler (unpublished).